Publication I

M. Takahashi, V. Pietilä, M. Möttönen, T. Mizushima, and K. Machida. 2009. Vortex-splitting and phase-separating instabilities of coreless vortices in *F*=1 spinor Bose-Einstein condensates. Physical Review A, volume 79, number 2, 023618, 10 pages.

# Vortex-splitting and phase-separating instabilities of coreless vortices in $F=1$ spinor Bose-Einstein condensates

M. Takahashi,[1] V. Pietilä,[2,4] M. Möttönen,[2,3,4] T. Mizushima,[1] and K. Machida[1]
[1]*Department of Physics, Okayama University, Okayama 700-8530, Japan*
[2]*Department of Applied Physics/COMP, Helsinki University of Technology, P. O. Box 5100, FI-02015 TKK, Finland*
[3]*Low Temperature Laboratory, Helsinki University of Technology, P. O. Box 3500, FI-02015 TKK, Finland*
[4]*Australian Research Council, Centre of Excellence for Quantum Computer Technology, The University of New South Wales, Sydney 2052, Australia*

(Received 4 December 2008; published 17 February 2009)

The low-lying excitations of coreless vortex states in $F=1$ spinor Bose-Einstein condensates (BECs) are theoretically investigated using the Gross-Pitaevskii and Bogoliubov–de Gennes equations. The spectra of the elementary excitations are calculated for different spin-spin interaction parameters and ratios of the number of particles in each sublevel. There exist dynamical instabilities of the vortex state which are suppressed by ferromagnetic interactions, and, conversely, enhanced by antiferromagnetic interactions. In both of the spin-spin interaction regimes, we find vortex-splitting instabilities in analogy with scalar BECs. In addition, a phase-separating instability is found in the antiferromagnetic regime.

DOI: 10.1103/PhysRevA.79.023618 PACS number(s): 03.75.Mn, 03.75.Kk, 03.75.Lm, 67.30.he

## I. INTRODUCTION

The realization of atomic Bose-Einstein condensates (BECs) [1–4] constituted the beginning of a new era in atomic physics. Compared with the traditional solid state systems, BECs in ultracold atomic gases have several appealing features, such as tunable interaction strengths, various trap potentials, and direct observation of the particle density. These properties offer a unique venue for many different types of studies such as the stability of the BECs in a trap potential, topological defects, multicomponent BECs, BECs in optical lattices, and low-dimensional Bose gases [5–7].

In this work, we focus on vortex states in spinor BECs [8,9], which have been realized experimentally in $^{23}$Na and $^{87}$Rb with the hyperfine spin states $F=1$ and 2 [10–15]. In these experiments, the atoms are confined optically and the condensate exhibits a genuine spin degree of freedom. Due to the $(2F+1)$ different hyperfine spin sublevels, the spinor BECs can have several topologically different stationary states, including vortex states. The quantized vortex is defined as a phase singularity of the condensate wave function [4]. The phase of the wave function winds by $2\pi n$ about the vortex core, where the integer $n$ is referred to as the vortex quantum number. For scalar BECs, the particle density vanishes at the vortex core due to diverging superfluid velocity. Due to the internal states in the spinor BECs, several types of vortices and other topological defects can be found. Studies related to these topological defects have been carried out experimentally in Refs. [16,17]. Theoretical studies of vortices and other topological defects in $F=1$ spinor BECs were initiated by Ohmi and Machida [8] and Ho [9]. Systematic investigations on vortices were followed by Yip [18] who considered both axisymmetric and nonaxisymmetric vortices, and by Isoshima *et al.* [19–22], who considered only axisymmetric vortices and their excitation spectra. Studies of different types of related topological defects have also been carried out in the literature: Leonhardt and Volovik [23], studied a defect referred to as Alice which is also known as the half quantum vortex. Stoof [24] and Marzlin *et al.* [25] studied so-called skyrmions. Mizushima *et al.* [26–28], Martikainen *et al.* [29], and Pietilä *et al.* [30] studied coreless vortices, also known as Mermin-Ho [31] or Anderson-Toulouse vortices [32]. In superfluid $^3$He-A, coreless vortices are typically referred to as continuous or analytic vortices and, for example, their existence [33] and circulation quantum [34] have been experimentally observed. Furthermore, other studies of the exotic properties of $F=1$ spinor BECs have carried out in Refs. [35–37]. For $F>1$, also many theoretical studies have been reported [38–45].

In this work, we consider the coreless vortex states in spinor BECs with hyperfine spin $F=1$. In the $z$-quantized basis, the condensate order parameter is denoted by $\phi_i$ where $i=1,0,-1$. For the coreless vortex state, the core of the vortex is filled by one of the components of the order parameter $\phi_i$. Thus the coreless vortex is fundamentally different from the vortex in scalar BECs. Typically, the coreless vortex state can be defined by a combination of winding numbers $\langle w_1,w_0,w_{-1}\rangle=\langle 0,1,2\rangle$ [26,30]. However, by changing the magnetization per particle $M$, analogous vortex states to the ones in a scalar BEC can be realized in the limit $M=-1$, since in this case the state $\phi_{-1}$ is fully populated. In this limit, the coreless vortex state of the condensate corresponds to a doubly quantized vortex in a scalar condensate which is known to be dynamically unstable [46–50,53–55]. The dynamical instability is characterized by the appearance of the complex-frequency eigenmodes in the excitation spectrum (see Sec. II). The existence of excitations with negative but real energy is referred to as energetic instability or local instability and it implies that there is a stationary state with smaller energy to which the system tends to decay in the presence of dissipation. On the other hand, the $M=1$ limit is a vortex-free state of a scalar BEC, which is the ground state in nonrotating systems. It is thus expected that the nature of the instability of the coreless vortex state changes as a function of $M$ between these two extreme limits.

Let us discuss the differences between the present and previous studies. The condensate phase diagram in a plane of

 

$M$ and external rotation $\Omega$ has been partially studied in Refs. [22,26,28]. Mizushima *et al.* [28] focused on the ground state properties in the range $0 \leqslant M \leqslant 1$, and Isoshima *et al.* [22] studied axisymmetric vortex states with winding numbers $w_i < 2$ in the range $-1 \leqslant M \leqslant 1$. However, these studies are not focused on the dynamical instability. The dynamical instability of the coreless vortex in a Ioffe-Pritchard magnetic field has been studied by Pietilä *et al.* [30], but only the ferromagnetic case was considered.

In this paper, we focus on the existence and characteristics of the dynamical instabilities in multicomponent systems. The coreless vortex state is an advantageous choice for these studies since each limit of the magnetization corresponds either to a dynamically unstable or stable state of a scalar BEC. We clarify how the dynamical instabilities of the coreless vortex state change as a function of magnetization $M$ in both ferromagnetic and antiferromagnetic interaction regimes. It is topical to study the antiferromagnetic regime since the coreless vortex state has been realized in $^{23}$Na atoms with $F=1$ using the topological phase imprinting method [16] according to the theoretical proposal [20,21]. On the other hand, $^{87}$Rb atoms in the $F=1$ hyperfine spin state constitutes a ferromagnetic BEC. We demonstrate different aspects of dynamical instabilities in these two interaction regimes. The dynamical instability is suppressed by the ferromagnetic interactions, whereas it is enhanced by the antiferromagnetic interactions. In the latter case, there are two kinds of dynamical instabilities: the vortex-splitting and phase-separating instabilities. In addition, we discuss the physical mechanisms behind these results.

This paper is organized as follows. In Sec. II, we introduce a theoretical description and details of the studied system. In Sec. III, we illustrate the condensate order parameter as a function of $M$ in different spin-spin interaction regimes and show a typical excitation spectrum including complex eigenvalues. Then we present our main results on the dynamical instabilities arising for different spin-spin interactions. In Sec. IV, we conclude our study. In the Appendix, we provide a proof of the existence of the so-called Kohn modes in the mean-field picture of spinor BECs.

## II. SYSTEM AND FORMULATION

We begin with the second quantized Hamiltonian for an $F=1$ spinor BEC [4] in the absence of a magnetic field,

$$\hat{H} = \int d\boldsymbol{r}\Bigg( \sum_i \hat{\Psi}_i^\dagger H_i^0 \hat{\Psi}_i + \frac{g_n}{2}\sum_{i,j} \hat{\Psi}_i^\dagger \hat{\Psi}_j^\dagger \hat{\Psi}_j \hat{\Psi}_i + \frac{g_s}{2}\sum_{i,j,k,l}\sum_\alpha \hat{\Psi}_i^\dagger \hat{\Psi}_j^\dagger (F_\alpha)_{i,l}(F_\alpha)_{j,k}\hat{\Psi}_k \hat{\Psi}_l \Bigg), \tag{1}$$

where

$$H_i^0 = -\frac{\hbar^2}{2m}\nabla^2 + V_{\mathrm{trap}}(\boldsymbol{r}) - \boldsymbol{\Omega}\cdot(-i\hbar\boldsymbol{r}\times\boldsymbol{\nabla}) - \mu_i, \tag{2}$$

and $\hat{\Psi}_i$ is the bosonic field operator in the $i$th spin sublevel and $m$ is the mass of the atoms. Here $(F_\alpha)_{i,j}$ is the $(i,j)$ component of the spin matrix $F_\alpha$ $(\alpha = x,y,z)$ for hyperfine spin $F=1$ system. The chemical potential is defined as $\mu_j = \mu + j\delta\mu$ in our calculation. The subscripts $\{i,j,k,l\}$ take values of the spin sublevels 1, 0, and $-1$. The strength of the density-density and spin-spin interactions are denoted by the coupling constants $g_n = 4\pi\hbar^2(a_0+2a_2)/3m$ and $g_s = 4\pi\hbar^2(a_2 - a_0)/3m$, respectively. Here $a_0$ and $a_2$ are the $s$-wave scattering lengths between atoms with total spin 0 and 2, respectively. In our calculation, the axisymmetric trap potential is $V_{\mathrm{trap}}(\boldsymbol{r}) = \frac{1}{2}m\omega^2 r^2$ with $r = \sqrt{x^2+y^2}$ and the external rotation is taken along the $z$ axis $\boldsymbol{\Omega} = (0,0,\Omega)$. We consider a uniform system along the $z$ direction.

Following the standard procedure [8,9], we write the time-dependent Gross-Pitaevskii (TDGP) equation as

$$i\hbar\frac{\partial\tilde{\psi}_i(\boldsymbol{r},t)}{\partial t} = \left(H_i^0 + g_n\sum_j |\tilde{\psi}_j(\boldsymbol{r},t)|^2\right)\tilde{\psi}_i(\boldsymbol{r},t) + g_s\sum_{j,k,l}\sum_\alpha (F_\alpha)_{j,l}(F_\alpha)_{i,k}\tilde{\psi}_j^*(\boldsymbol{r},t)\tilde{\psi}_k(\boldsymbol{r},t)\tilde{\psi}_l(\boldsymbol{r},t). \tag{3}$$

Here, the field operator $\hat{\Psi}_i$ has been replaced by its expectation value $\tilde{\psi}_i(\boldsymbol{r},t) = \langle\hat{\Psi}_i(\boldsymbol{r},t)\rangle$. In our simulations, we find the stationary state $\phi_i(\boldsymbol{r})$ using imaginary time propagation.

In an axisymmetric configuration, the wave function can be decomposed into the amplitude and phase factor as

$$\phi_i(\boldsymbol{r}) = \phi_i'(r)\gamma_i(\theta) = \phi_i'(r)\exp[i(\alpha_i + w_i\theta)]. \tag{4}$$

Following the arguments of Isoshima *et al.* [22], stationary states obey the conditions

$$2\alpha_0 = \alpha_1 + \alpha_{-1} + n\pi, \tag{5}$$

$$2w_0 = w_1 + w_{-1}, \tag{6}$$

with $n \in \mathbb{Z}$. In Eq. (5), we choose $n=0$, $\alpha_0 = \alpha_{\pm 1} = 0$ for the ferromagnetic interaction, and $n=1$, $\alpha_0 = \pi/2$, $\alpha_{\pm 1} = 0$ for the antiferromagnetic case, without loss of generality. Hence, we can choose $\{\phi_i'\}$ to be real positive valued functions in the following discussion. These choices have essentially no effect in the discussion below. Note that the coreless vortex states are defined as $\langle w_1, w_0, w_{-1}\rangle = \langle 0,1,2\rangle$, which satisfies Eq. (6).

Let us consider small fluctuations in the vicinity of the stationary state $\phi$:

$$\psi_i(\boldsymbol{r},t) = \phi_i(\boldsymbol{r}) + \lambda[u_{\boldsymbol{q},i}(\boldsymbol{r})e^{i(E_{\boldsymbol{q}}/\hbar)t} - v_{\boldsymbol{q},i}^*(\boldsymbol{r})e^{-i(E_{\boldsymbol{q}}^*/\hbar)t}]. \tag{7}$$

By linearizing Eq. (3) with respect to $\lambda$, we obtain the Bogoliubov–de Gennes (BdG) equation,

$$\hat{T}\boldsymbol{w}_{\boldsymbol{q}} = E_{\boldsymbol{q}}\boldsymbol{w}_{\boldsymbol{q}} \tag{8}$$

where the BdG operator $\hat{T}$ is composed of $3\times 3$ complex matrices $\underline{P}$ and $\underline{Q}$,

$$\hat{T} \equiv \begin{bmatrix} \underline{P} & -\underline{Q} \\ \underline{Q}^* & -\underline{P}^* \end{bmatrix}. \tag{9}$$

The matrix elements of $\underline{P}$ and $\underline{Q}$ are given by [19]

$$P_{i,j} = H_i^0 \delta_{i,j} + g_n\left(\phi_i\phi_j^* + \sum_k |\phi_k|^2 \delta_{i,j}\right) + g_s \sum_{k,l} \sum_{\alpha} [(F_\alpha)_{k,j}(F_\alpha)_{i,l} + (F_\alpha)_{k,l}(F_\alpha)_{i,j}]\phi_k^*\phi_l, \tag{10}$$

$$Q_{i,j} = g_n\phi_i\phi_j + g_s \sum_{k,l} \sum_{\alpha} (F_\alpha)_{j,k}(F_\alpha)_{i,l}\phi_k\phi_l. \tag{11}$$

In Eq. (8), the eigenfunction is denoted by

$$\boldsymbol{w}_q = \begin{bmatrix} \boldsymbol{u}_q \\ \boldsymbol{v}_q \end{bmatrix}, \quad \boldsymbol{u}_q = \begin{bmatrix} u_{q,1} \\ u_{q,0} \\ u_{q,-1} \end{bmatrix}, \quad \boldsymbol{v}_q = \begin{bmatrix} v_{q,1} \\ v_{q,0} \\ v_{q,-1} \end{bmatrix}. \tag{12}$$

Since the BdG matrix (9) is generally non-Hermitian, the eigenvalues $E_q$ can be complex.

The BdG matrix has two symmetries

$$\hat{T}^* = -\hat{\tau}_1 \hat{T} \hat{\tau}_1, \tag{13}$$

and

$$\hat{T}^\dagger = \hat{\tau}_3 \hat{T} \hat{\tau}_3, \tag{14}$$

where we have introduced the first and third Pauli matrices as $\hat{\tau}_1 \equiv \left[\begin{smallmatrix} \underline{0} & \underline{\tau}_0 \\ \underline{\tau}_0 & \underline{0} \end{smallmatrix}\right]$ and $\hat{\tau}_3 \equiv \left[\begin{smallmatrix} \underline{\tau}_0 & \underline{0} \\ \underline{0} & -\underline{\tau}_0 \end{smallmatrix}\right]$, where $\underline{\tau}_0 \equiv \mathrm{diag}(1,1,1)$ and $\underline{0}$ is a $3\times 3$ matrix of zeros. The first symmetry in Eq. (13) implies the existence of two symmetric eigenmodes

$$(E_q, \boldsymbol{w}_q) \Leftrightarrow (-E_q^*, \hat{\tau}_1 \boldsymbol{w}_q^*). \tag{15}$$

These modes have opposite angular momenta under the axial symmetry.

Using the second symmetry in Eq. (14), we obtain

$$(E_q^* - E_{q'}) \int d\boldsymbol{r}\, \boldsymbol{w}_q^\dagger(\boldsymbol{r}) \hat{\tau}_3 \boldsymbol{w}_{q'}(\boldsymbol{r}) = 0. \tag{16}$$

For a real eigenvalue $E_q^* = E_q$, Eq. (16) implies that for $\boldsymbol{q} \neq \boldsymbol{q}'$ the two modes are orthogonal. Thus we use the normalization

$$\int d\boldsymbol{r}\, \boldsymbol{w}_q^\dagger(\boldsymbol{r}) \hat{\tau}_3 \boldsymbol{w}_{q'}(\boldsymbol{r}) = \delta_{q,q'} \tag{17}$$

for quasiparticle amplitudes corresponding to real eigenvalues of the BdG equation. Two modes provided by the symmetry in Eq. (13) give identical contributions to the energy of the quasiparticles and thus only the mode with positive norm in Eq. (17) is chosen as a physically meaningful mode.

In the case of the complex eigenvalue $E_q^* \neq E_q$, Eq. (16) gives $\int d\boldsymbol{r}\, \boldsymbol{w}_q^\dagger \hat{\tau}_3 \boldsymbol{w}_q = 0$ and we take the following normalization condition [56]:

$$\int d\boldsymbol{r}\, \boldsymbol{w}_q^\dagger(\boldsymbol{r}) \hat{\tau}_3 \bar{\boldsymbol{w}}_{q'}(\boldsymbol{r}) = \delta_{q,q'}. \tag{18}$$

We use a pair of eigenmodes $(E_q, \boldsymbol{w}_q)$ and $(\bar{E}_q, \bar{\boldsymbol{w}}_q)$, for which the eigenvalues satisfy the condition $E_q^* = \bar{E}_q$. We can find such an eigenmode as follows. By introducing a unitary matrix $\hat{U} \equiv \mathrm{diag}[\underline{A}, \underline{A}^*]$, where $\underline{A} \equiv e^{i\alpha_1}\mathrm{diag}[1, e^{i\alpha}, e^{2i\alpha}]$, and $\alpha \equiv \alpha_0 - \alpha_1$, which renders the BdG matrix (9) real, Eq. (8) can be written in the form

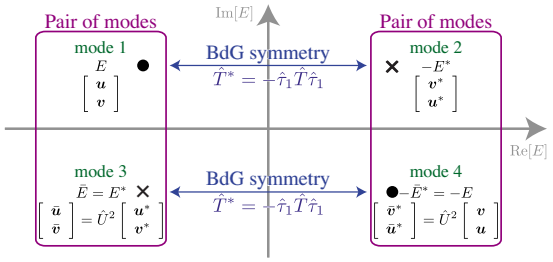


FIG. 1. (Color online) A set of complex-frequency modes in the complex plane. Four complex-frequency modes exist together.

$$\hat{T}' \boldsymbol{x}_q = E_q \boldsymbol{x}_q, \tag{19}$$

where $\hat{T}' = \hat{U}^\dagger \hat{T} \hat{U}$ is a real matrix. The complex conjugate of the equation assumes the form

$$\hat{T}' \boldsymbol{x}_q^* = E_q^* \boldsymbol{x}_q^*, \tag{20}$$

For a real eigenvalue $E_q^* = E_q$, the eigenfunction can be taken to be real $\boldsymbol{x}_q^* = \boldsymbol{x}_q$. Hence Eqs. (19) and (20) are identical. For a complex eigenvalue $E_q^* \neq E_q$, the eigenfunction $\boldsymbol{x}_q$ is complex, i.e., $\boldsymbol{x}_q^* \neq \boldsymbol{x}_q$. The eigenfunctions in Eq. (19) and (20) are $\boldsymbol{x}_q = \hat{U}^\dagger \boldsymbol{w}_q$ for $E_q$ and $\boldsymbol{x}_q^* = \hat{U}\boldsymbol{w}_q^*$ for $E_q^*$, where we used $U^* = U^\dagger$. Here $(E_q, \boldsymbol{w}_q)$ is a solution of the eigenvalue equation (8). For a complex $E_q$, the eigenstates in Eq. (8) appear as a pairs $(E_q, \boldsymbol{w}_q)$ and $(E_q^*, \bar{\boldsymbol{w}}_q)$, where $\bar{\boldsymbol{w}}_q = \hat{U}^2 \boldsymbol{w}_q^*$. The additional factor $\hat{U}^2$ in $\bar{\boldsymbol{w}}_q$ changes the relative phase between spin components.

By choosing the normalization condition Eq. (18) for complex eigenmodes, one can construct a complete set with the complex-frequency modes [56]. The normalization condition in Eq. (18) leaves the relative amplitude between $\boldsymbol{w}_q$ and $\bar{\boldsymbol{w}}_q$ as well as their phase undetermined. In our study, we take equal amplitudes for $\boldsymbol{w}_q$ and $\bar{\boldsymbol{w}}_q$, that is, $|u_{q,i}(\boldsymbol{r})| = |\bar{u}_{q,i}(\boldsymbol{r})|$ and $|v_{q,i}(\boldsymbol{r})| = |\bar{v}_{q,i}(\boldsymbol{r})|$. The physical interpretation of the quasiparticle amplitudes $\boldsymbol{w}_q$ and $\bar{\boldsymbol{w}}_q$ corresponding to a complex eigenvalue is still an open question [57].

The summary of the complex-frequency modes is shown in Fig. 1, where we omit quantum indices in the figure. Modes 1 and 2 as well as modes 3 and 4 are linked by the symmetry in Eq. (13). Modes 1 and 3 and modes 2 and 4 in Fig. 1 are used to construct the normalization condition in Eq. (18) for a complex eigenvalue $E_q^* \neq E_q$. For the complex-frequency eigenmodes, the two modes that satisfy the conservation of the energy and angular momentum are in resonance with each other (see Sec. III B for details).

For an axially symmetric system, all the eigenmodes of Eq. (8) can be classified with the quantum number $q_\theta \in \mathbb{Z}$ denoting the angular momentum with respect to the condensate. The eigenfunction is thus of the form

$$u_{q,i}(\boldsymbol{r}) = u_{q,i}(r)\exp[i(q_\theta + w_i)\theta], \tag{21}$$

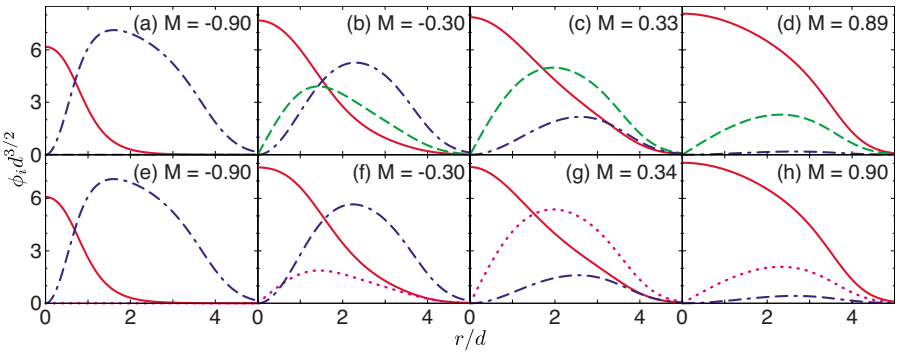


FIG. 2. (Color online) Spatial profile of the order parameter for $g_s'=-0.001$ (a)–(d) and for $g_s'=0.001$ (e)–(h). The magnetization $M$ is (a) −0.90, (b) −0.30, (c) 0.33, (d) 0.89, (e) −0.90, (f) −0.30, (g) 0.34, and (h) 0.90. The solid, dashed, and dash-dotted lines correspond to the $m_F=1$, 0, and −1 components, respectively. The order parameter corresponding to the $m_F=0$ component in the antiferromagnetic case, denoted by the dotted line, is purely imaginary.

$$v_{\boldsymbol{q},i}(\boldsymbol{r}) = v_{\boldsymbol{q},i}(r)\exp[i(q_\theta - w_i)\theta]. \tag{22}$$

We solve the BdG equation using the decomposition of Eqs. (21) and (22) to obtain the spectrum of the low-lying excitations.

From this point on, we use dimensionless quantities. The energy is normalized by the trap energy $\hbar\omega$, and the length is normalized by $d \equiv \sqrt{\hbar/m\omega}$. In our study, we choose the density-density coupling constant as $g_n' \equiv g_n/(\hbar\omega d^3) = 0.113$, and spin-spin coupling constant as $g_s' \equiv g_s/(\hbar\omega d^3) = \pm 0.001$, $\pm 0.01$. The negative values of $g_s$ correspond to the ferromagnetic case and the positive ones to the antiferromagnetic case. The values of the coupling constants $g_n'$ and $g_s'$ in the physical system [58,59] can be varied by tuning the trap frequency. In addition, $g_n$ can be changed by using Feshbach resonances, and hence the ratio of $g_n$ and $g_s$ is also adjustable. We note that a drawback in utilizing the standard dc Feshbach resonance is that it tends to fix the magnetization of the cloud because of a required strong magnetic field. We assume an infinitely long axisymmetric system along the $z$ axis, which renders the numerical problem two dimensional. Alternatively, our results apply to pancake-shaped condensates, for which the coherent dynamics in the tight direction can be neglected. Here, cylindrical coordinate $\boldsymbol{r}=(r,\theta,z)$ is introduced and the integration in the two-dimensional plane is denoted as $\int_{2D} d\boldsymbol{r} \equiv \int r\, dr \int \sin\theta\, d\theta$. The total number of the atoms $N \equiv \Sigma_i \int_{2D} d\boldsymbol{r} |\phi_i|^2 = 1.5 \times 10^3 d^{-1}$ is fixed. With this set of values of $g_n'$ and $N$, doubly quantized vortex states in scalar BECs have a dynamical instability [46–49]. The magnetization is obtained from $M \equiv \int_{2D} d\boldsymbol{r}(|\phi_1|^2 - |\phi_{-1}|^2)/N$.

For low enough rotation frequencies, vortex lattices do not form, and hence Eq. (4) holds. Thus the effect of the external rotation can be taken into account as a chemical potential shift such that $\mu_j' \equiv \mu' + j\delta\mu'$, $\mu' \equiv \mu + \hbar\Omega$, and $\delta\mu' \equiv \delta\mu - \hbar\Omega$. In experiments, the magnetization per particle, $M$, is an observable, and hence the chemical potentials $\mu_i$ can be treated as Lagrange multipliers in the calculation. Thus, the rotation cannot change the Gross-Pitaevskii (GP) solution under constant $M$. On the other hand, the external rotation changes the excitation spectrum by $\Delta E_{\boldsymbol{q}}(\Omega) \equiv E_{\boldsymbol{q}}(\Omega) - E_{\boldsymbol{q}}(\Omega=0) = -\hbar\Omega q_\theta$.

## III. RESULTS

### A. Coreless vortex states

We study the coreless vortex states, defined by the combination of the phase windings of each component $\langle w_1, w_0, w_{-1}\rangle = \langle 0,1,2\rangle$, for magnetization ranging from −1 to 1, and for different strengths of the spin-spin interaction. In Fig. 2, we display typical spatial profiles of the order parameter for $g_s'=-0.001$ and 0.001. In Fig. 3, the particle number $N_i$ in different hyperfine spin states is presented as a function of $M$ for different values of the spin-spin coupling constant $g_s'$.

According to Isoshima *et al.* [22], the spin-dependent term of the energy density functional can be written as

$$E_s(r) \equiv \frac{g_s'}{2}\{2\phi_0'^2(r)[\phi_1'(r) \pm \phi_{-1}'(r)]^2 + [\phi_1'^2(r) - \phi_{-1}'^2(r)]^2\}. \tag{23}$$

Here we have assumed the phase condition $\gamma_1\gamma_{-1}\gamma_0^{*2} = \pm 1$ which stems from the requirement that the spin-dependent

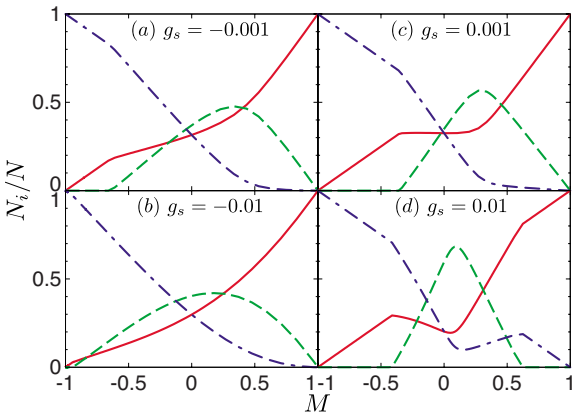


FIG. 3. (Color online) The ratio of the atoms in hyperfine spin states and total number of the atoms $N_i/N$ as a function of magnetization for $g_s'$ equals to (a) −0.001, (b) −0.01, (c) 0.001, and (d) 0.01. The solid, dashed, and dash-dotted lines correspond to $m_F=1$, 0, and −1 components, respectively. The total number of atoms in the two-dimensional (2D) plane is fixed to $N=1.5\times 10^3 d^{-1}$.

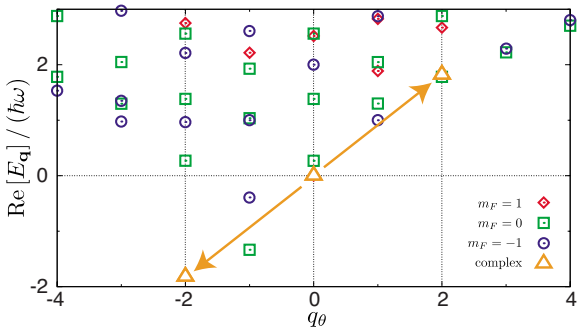


FIG. 4. (Color online) Excitation spectrum for $M=-0.9$ and $g_s'=-0.001$. The triangle at $[q_\theta=0, \mathrm{Re}(E_q)=0]$ corresponds to the GP solution. The labels indicate the majority component in the quasiparticle amplitudes $u_i$ and $v_i$. This spectrum includes the complex-frequency modes denoted by the triangles at $[q_\theta=\pm 2, \mathrm{Re}(E_q)=\pm 1.82]$.

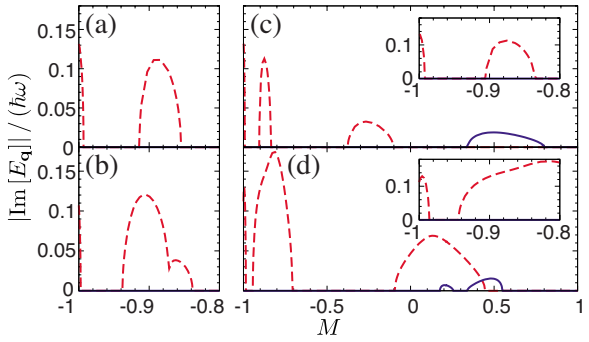


FIG. 5. (Color online) The absolute values of the imaginary parts of the complex-frequency eigenvalues are shown as a function of the magnetization $M$ for $g_s'$ equals to (a) −0.001, (b) −0.01, (c) 0.001, and (d) 0.01. The $q_\theta=\pm 2$ and $\pm 1$ modes are indicated by dashed and solid lines, respectively. The insets in (c) and (d) show the detailed structure in the vicinity of $M=-1$ for $g_s'=0.001$ and 0.01. There are no complex-frequency modes found for $M>-0.8$ in the ferromagnetic case.

part of the total energy is minimized. The upper (lower) sign corresponds to ferromagnetic (antiferromagnetic) interaction. Equation (23) helps to understand the $M$ dependence of the order parameter for different values of $g_s'$. In terms of Eq. (23), a large magnitude of the spin vector is more favorable in the ferromagnetic case, and oppositely, in the antiferromagnetic case, the spin vector tends to vanish. By comparing Figs. 2(b) and 2(f), we observe that $\phi_0$ has larger amplitude in the ferromagnetic case and therefore enhances the magnitude of the spin vector. Furthermore, for a broad range of $M$, $N_0$ is finite in the ferromagnetic case whereas it typically vanishes for antiferromagnetic interactions as shown in Fig. 3. Moreover, the fact that the $m_F=-1$ component has a different winding number to $m_F=1$ component explains the asymmetry of the distributions in Fig. 3.

### B. Excitation spectra and complex-frequency modes

We present a typical excitation spectrum to explain the mechanism behind the appearance of the dynamical instabilities. As observed from Eq. (7), the fluctuation term grows exponentially in time when some eigenvalue $E_q$ is complex. This is referred to as the dynamical instability. In this case, small perturbations about the stationary solution of the GP equation can render it to decay into another state even in the absence of dissipation.

A typical excitation spectrum including complex-frequency modes is shown in Fig. 4. In this figure, the horizontal axis is the angular momentum quantum number $q_\theta$ of the excited state and the vertical axis is the real part of the excitation energy $\mathrm{Re}(E_q)$. The eigenstate at $q_\theta=0$ and $E_q=0$ corresponds to the GP solution. The excitation modes are labeled by the majority component of the excitation, that is, for the excitation with label $m_F=i$, the largest amplitude of the fluctuation is given by $\int_{2D} d\boldsymbol{r}(|u_i|^2+|v_i|^2)$.

The excitation spectrum shown in Fig. 4 corresponds to $g_s'=-0.001$ and $M=-0.9$. In this case, the state derived from the GP equation has most of the particles occupying the $m_F=-1$ component with a winding number $w_{-1}=2$ and a small amount of $m_F=1$ component fills the core of the vortex in the $\phi_{-1}$ component; see Fig. 2(a).

The labels also illustrate the nature of the excitation modes. For example, in the $M=-1$ limit, the $m_F=1$, 0, and $-1$ modes correspond to longitudinal spin fluctuations, transverse spin fluctuations, and density fluctuations. However, apart from this limit, the excitation modes are more complicated, because of the mixing between different spin components.

In the spontaneous dynamical excitation of the complex-frequency modes, conservation of the total energy and angular momentum must be satisfied. As depicted in Fig. 4, the pair of complex-frequency modes with $[q_\theta=-2, \mathrm{Re}(E_q)=-1.82]$ and $[q_\theta=2, \mathrm{Re}(E_q)=1.82]$ satisfies the aforementioned constraints, and hence the initial state with $[q_\theta=0, \mathrm{Re}(E_q)=0]$ can spontaneously decay into these two states without any dissipation. There are also additional restrictions for the appearance of the complex-frequency modes which will be discussed later. We also note that external rotation does not affect this condition since the excitation energies are shifted by $-\hbar\Omega q_\theta$ (see Sec. II).

Several complex-frequency modes are found in both ferromagnetic and antiferromagnetic cases. Figure 5 presents the imaginary part of the eigenvalues as a function of $M$. We find that two types of complex-frequency modes can appear in the coreless vortex states: (i) a pair of $q_\theta=\pm 2$ modes, and (ii) a pair of $q_\theta=\pm 1$ modes. The former complex-frequency mode appears in the vicinity of $M=-1$ in both ferromagnetic and antiferromagnetic cases as shown in Fig. 5. The results in the $M=-1$ limit reproduce those of the doubly quantized vortex in a scalar BEC [46–50]. In contrast, another pair of complex-frequency modes with $q_\theta=\pm 1$ emerges in the antiferromagnetic interaction regime.

Figure 6 shows the excitation energies of the $q_\theta=\pm 2$ modes for $g_s'=-0.001$ as a function of $M$. The solid, dashed, and dash-dotted lines correspond to $q_\theta=2$ modes, for which the majority components are $m_F=1$, 0, and $-1$, respectively. The eigenenergy of the $q_\theta=-2$ mode is plotted as $-\mathrm{Re}(E_q)$ and denoted by dots. The majority component for this excitation is $m_F=-1$. The complex-frequency modes appear in the regions where $q_\theta=2$ and $q_\theta=-2$ modes overlap, due to

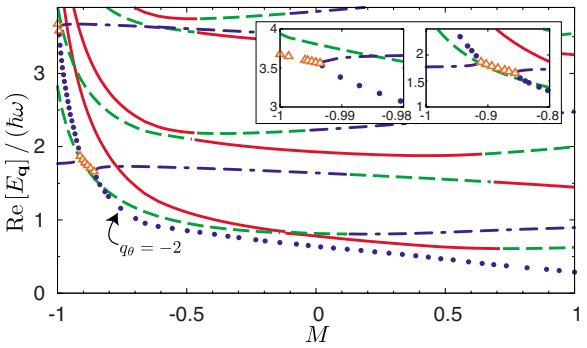


FIG. 6. (Color online) Magnetization dependence of the excitation energies of the $q_\theta = \pm 2$ modes for $g_s' = -0.001$. The insets show the details of the spectrum where complex eigenenergies appear. The eigenenergy of the $q_\theta = -2$ mode is plotted as $-\mathrm{Re}(E_{\boldsymbol{q}})$. The majority component in the quasiparticle amplitudes $u_i$ and $v_i$ of the corresponding excitation energies is indicated by the solid, dashed, and dash-dotted lines for the $m_F = 1$, 0, and $-1$ components in $q_\theta = 2$ mode, respectively. The dots indicate $q_\theta = -2$ mode, which is dominated by the $m_F = -1$ component. The complex-frequency modes are labeled by triangles in both $q_\theta = \pm 2$ modes.

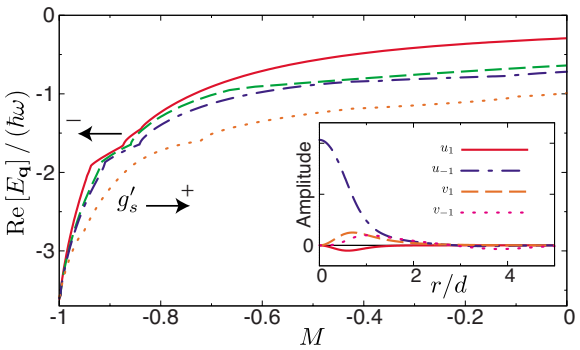


FIG. 7. (Color online) Magnetization dependence of the lowest-energy excitations with $q_\theta = -2$ for different values of $g_s'$. The solid, dashed, dash-dotted, and dotted lines indicate the $g_s' = -0.01$, $-0.001$, 0.001, and 0.01 cases, respectively. The shift toward positive energy increases with $g_s'$ decreasing from positive to negative values. The inset shows the absolute values of the quasiparticle amplitudes $\{u_i, v_i\}$ for $g_s = -0.001$ and $M = -0.95$. $u_0$ and $v_0$ are neglected since they are vanishingly small.

the energy and angular momentum constraints.

Let us discuss the dependence of $q_\theta = 2$ modes shown in Fig. 6. These modes are classified as quadrupole modes, which give rise to the two-fold rotational symmetric deformation of the condensate. In spinor BECs, due to the multicomponent sublevels of the order parameter, there are three kinds of quadrupole modes: the transverse and longitudinal spin quadrupole modes and the density quadrupole mode, which correspond to the three lowest lines around $M = 1$ in Fig. 6, respectively. The other modes with higher energy are the higher order quadrupole modes. The lowest density fluctuation mode with $q_\theta = 2$ is embed at $E_{\boldsymbol{q}} = 1.45\hbar\omega$ around $M = 1$, which is in good agreement with $E_{\boldsymbol{q}} = \sqrt{2}\hbar\omega$ derived within the Thomas-Fermi approximation [51]. With increasing $M$, since the ground state has a finite angular momentum $\langle l_z \rangle$ associated with the windings $\langle 0,1,2 \rangle$, the energy gradually shifts as $E_{\boldsymbol{q}}(M) - E_{\boldsymbol{q}}(M=1) \propto \langle l_z \rangle$ [52] and stays around $E_{\boldsymbol{q}} = 1.5\hbar\omega$ in the whole $M$ region. We also note that the energy of the transverse and longitudinal quadrupole modes, which are shown with solid and dashed lines near $M = -1$, rapidly increase as $M$ decreases because of the increase of the relative chemical potential difference $\delta\mu$. Since the energy of the lowest excitations with $q_\theta = -2$ increases with $M$ near $M = -1$ and the resonating $q_\theta = 2$ density quadrupole mode remains almost constant, the complex-frequency modes eventually disappear, as shown in Fig. 6. The complex-frequency modes appear again near $M = -0.9$ since the $q_\theta = -2$ excitation mode finds another mode to pair with such that the total energy and angular momentum conservations are satisfied.

The complex-frequency modes appear for a clearly wider range of values of $M$ in the antiferromagnetic case compared with the ferromagnetic case [see Figs. 5(a) and 5(b) and insets of Figs. 5(c) and 5(d)]. To explain this tendency, we consider the lowest negative energy excitation with $q_\theta = -2$. The excitation energy increases faster with increasing $M$ in the ferromagnetic case as shown in Fig. 7. This tendency results from the spatial profile for the $q_\theta = -2$ mode. The lowest-energy excitation with $q_\theta = -2$ is mainly composed of the $u_{-1}$ wave function as shown in the inset of Fig. 7. The excitation wave function can be generally expanded in terms of the $q$th Bessel function $J_q(r)$ as $u_{\boldsymbol{q},i}(r) = \Sigma_{s=1}^{\infty} A_s J_{q_\theta + w_i}(k_s r)$, where $k_s = \lambda_s / L$. Here $\lambda_s$ is the zero point of the Bessel function and $L$ is the cutoff length of the system. Since the Bessel function behaves as $J_q(r) \sim r^{|q|}$ near $r = 0$, and $q_\theta + w_{-1} = 0$, we have $u_{-1} \propto r^0$ near $r = 0$. Hence, the lowest eigenmode at $q_\theta = -2$ is the core localized mode and the quasiparticle amplitude $u_{-1}(r)$ spatially overlaps with $\phi_1$, and fills the vortex core. Due to the coupling term $-g_s|\phi_1|^2 u_{-1}$ in the BdG matrix (9), the lowest eigenvalue increases rapidly in the ferromagnetic regime. In addition, the slope near $M = -1$ in Fig. 7 is steeper in the ferromagnetic case than in the antiferromagnetic case. The $q_\theta = 2$ modes with positive $\mathrm{Re}(E_{\boldsymbol{q}})$ in resonance with lowest $q_\theta = -2$ mode are less sensitive to changes in $M$, as we have discussed above. Hence, the complex-frequency eigenmode can appear only in narrow magnetization regions in the case of ferromagnetic interactions. Apart from $M \sim -1$, in the ferromagnetic case, the coreless vortex becomes dynamically stable.

Let us consider the difference in the density fluctuations induced by the two complex-frequency modes. The perturbed density profile of each component is shown in Fig. 8, where the first and second rows show the density fluctuations caused by the complex-frequency modes with $q_\theta = \pm 2$ and $q_\theta = \pm 1$, respectively. From the left to the right column, the densities of the $m_F = 1, 0, -1$ components are shown. The $m_F = 0$ component of the $q_\theta = \pm 2$ complex-frequency mode is neglected, because its amplitude is vanishingly small.

The $q_\theta = \pm 2$ complex-frequency mode breaks the doubly quantized vortex in the $m_F = -1$ component into two singly quantized vortices, as shown in Fig. 8(b). This mechanism of dynamical instability is equivalent to the dynamical instability of a doubly quantized vortex in scalar BECs. It has also been found in the studies of coreless vortices induced by external magnetic fields [30]. On the other hand, the $q_\theta = \pm 1$ complex-frequency mode, which appears only in the

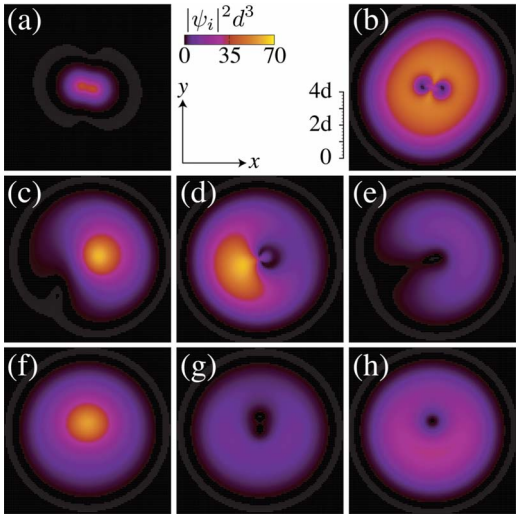


FIG. 8. (Color online) Density profiles $|\Psi_1|^2$ (left column), $|\Psi_0|^2$ (center column), and $|\Psi_{-1}|^2$ (right column) perturbed by excitation modes. The upper row corresponds to the complex-frequency $q_\theta = \pm 2$ modes for $g_s' = -0.001$ and $M = -0.9$, the middle row to the complex-frequency $q_\theta = \pm 1$ modes for $g_s' = 0.01$ and $M = 0.2$, and the lower row to the lowest real-frequency $q_\theta = -1$ mode for $g_s' = 0.01$ and $M = 0.3$. The density profile of the $m_F = 0$ component $|\Psi_0|^2$ in the upper row is neglected since it is vanishingly small. The complex modes with both positive and negative $q_\theta$ are equally superposed since the modes appear as a result of the energy and angular momentum conservation. The field of view is $10d \times 10d$. We take $\lambda = 100$ to show the essential qualitative features of the fluctuation.

antiferromagnetic regime, has a fundamentally different response on the condensate. We categorize this kind of dynamical instability mode as phase separation, since this mode leads to a spatial separation of the could into domains of a certain component $\phi_1$, $\phi_{-1}$ or $\phi_0$. Although the separation is not very sharp, it is clearly visible in Fig. 8. Furthermore, the $m_F = 1$ and $-1$ components tend to spatially overlap with each other, which is attributed to the attractive interaction between them due to the antiferromagnetic interaction, as seen in Eq. (23).

### C. Stable modes

In addition to the dynamical instabilities, there are modes with real eigenvalues even if the restrictions of the conservation of the total energy and angular momentum are satisfied. For example, (i) $q_\theta = \pm 2$ modes for $g_s' = -0.001$ near $M = -0.85$ are shown in Fig. 9(a), and (ii) $q_\theta = \pm 1$ modes for $g_s' = 0.01$ near $M = 0.3$ in Figs. 9(c) and 9(d).

Let us first consider the case (i). The corresponding modes have the $m_F = -1$ component in the majority for the $q_\theta = -2$ mode and $m_F = 0$ for the $q_\theta = 2$ mode. In particular, they satisfy the condition of the conservation of the total energy and angular momentum. Thus they can in principle form an excitation with complex eigenvalues, and in fact this is the case for $g_s' = -0.01$ and certain values of $M$ as shown in Fig. 9(b). The difference between these two cases can be traced back to the stationary solution of the GP equation.

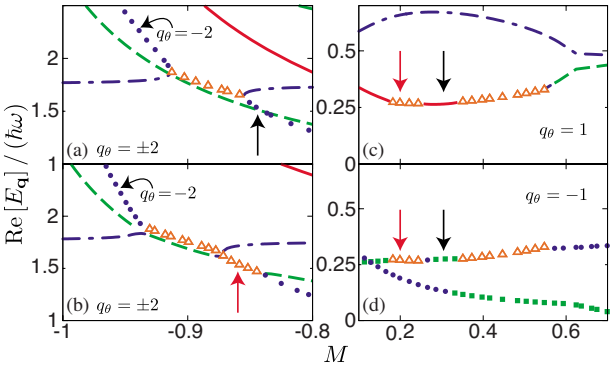


FIG. 9. (Color online) Detailed structures of the excitation spectra. We show $q_\theta = \pm 2$ modes for $g_s' = -0.001$ (a) and $-0.01$ (b), and $q_\theta = 1$ (c) and $-1$ (d) modes for $g_s' = 0.01$. The eigenenergies for $q_\theta = -2$ and $-1$ are plotted as $-\mathrm{Re}(E_q)$. For $q_\theta = 2$ and 1 modes, the majority components of the spectrum are indicated by solid, dashed, and dash-dotted lines corresponding to $m_F = 1$, 0, and $-1$, respectively. For the $q_\theta = -2$ and $-1$ modes, these are indicated by filled squares and dots corresponding to the $m_F = 0$ and $-1$ components, respectively. The complex-frequency modes are labeled by triangles in all cases.

According to Figs. 3(a) and 3(b), $\phi_0$ remains negligible for $M \lesssim -0.65$ and $g_s' = -0.001$, but $\phi_0$ is finite in the overlapping region for $g_s' = -0.01$. Hence the existence of a finite number atoms in the corresponding $q_\theta > 0$ mode can be considered as another restriction for the appearance of the dynamical instability.

Next, we move to the case (ii). In Figs. 9(c) and 9(d), we show excitations with purely real eigenfrequencies at $M \sim 0.3$ surrounded by excitations corresponding to complex eigenvalues. To understand this behavior, we consider the related density fluctuations. The density profiles in the case (ii) are shown in Figs. 8(f)–8(h). We notice that the fluctuation leads to the precession motion of the $\langle 0, 1, 2 \rangle$ coreless vortex and the phase separation appearing for $M = 0.2$ [Figs. 8(c)–8(e)] does not occur here. Hence we argue that the phase separation is a characteristic feature of this particular type of dynamical instability.

In addition to the above discussion on the existence of complex-frequency modes, we note that the existence of dipole modes is a general feature of the excitation spectrum of a harmonically trapped many-particle system. A generalization [60,61] of Kohn's theorem [62] shows that these center-of-mass oscillation modes should exist for scalar particles with energy eigenvalue $E_q = \hbar\omega$ independent of the interaction strength. Thus the existence of Kohn modes in the theory describing the system is typically used to check for the validity of the approximations made. It turns out that the dipole modes have exactly the energy $\hbar\omega$ in the finite-temperature Bogoliubov approximation, in which the spatial dependence of thermal gas component is neglected in the GP and BdG equations. For so-called Popov and second-order finite-temperature mean-field theories, the excitation energy is very close to, although not exactly, the trap energy [63]. In the Appendix, we present a proof that Kohn modes with energy $E_q = \hbar\omega$ exist for the BdG equations we utilize, independent of the magnetization, density-density, or spin-spin interactions.

## IV. CONCLUSIONS

We have investigated the stability of the coreless vortex states in $F=1$ spinor Bose-Einstein condensates; namely, we have calculated the low-energy excitation spectra in the whole range of magnetization $M$ by solving the Gross-Pitaevskii and the Bogoliubov–de Gennes equations. The complex-frequency modes, which cause the dynamical instabilities, have been found in both ferromagnetic and antiferromagnetic cases.

The complex-frequency modes in the ferromagnetic case cause the doubly quantized vortex to decay into a pair of singular vortices. In addition, antiferromagnetic interactions were found to cause phase separation through dynamical instability of coreless vortices. In general, we found that the dynamical instabilities tend to be suppressed by the ferromagnetic interactions and oppositely enhanced by the antiferromagnetic ones. We also note that a rather slow external rotation does not have an effect on the dynamical instabilities for a fixed magnetization.

In addition to the conventional energy and angular momentum conservation, we found other restrictions for the appearance of the dynamical instability. One such restriction for the $q_\theta>0$ mode is the need for a considerable particle number in the component of the condensate order parameter to be excited. Furthermore, we found that only certain $q_\theta<0$ modes can resonate with other modes. These correspond to the vortex-splitting mode with $q_\theta=-2$ in both interaction regimes, and the phase-separating mode with $q_\theta=-1$ in the antiferromagnetic regime. Due to these constraints, a dynamically stable coreless vortex can exist for certain magnetizations $M$, not only in the ferromagnetic case but also in the antiferromagnetic case. Our studies can be verified experimentally in fully optically trapped spinor BECs using present-day techniques.

## ACKNOWLEDGMENTS

We thank M. Mine and J. A. M. Huhtamäki for useful discussions. This work was supported by a grant of the Japan Society for the Promotion of Science (M.T., T.M., and K.M.), the Jenny and Antti Wihuri Foundation (V.P.), the Academy of Finland (M.M.), and Emil Aaltonen's Foundation (M.M. and V.P.).

## APPENDIX: EXISTENCE OF KOHN MODES

Here, we show that dipole modes exist in harmonically trapped spinor Bose-Einstein condensates described by the employed mean-field theory. We consider a general system at zero temperature. The single-particle Hamiltonian is defined as

$$H_0(\boldsymbol{r}) = -\frac{\hbar^2}{2m}\nabla^2 + V_{\mathrm{trap}}(\boldsymbol{r}), \tag{A1}$$

where $V_{\mathrm{trap}}(\boldsymbol{r})$ is a general three-dimensional harmonic trap potential, and $V_{\mathrm{trap}}(\boldsymbol{r})=\frac{1}{2}m\Sigma_\alpha\omega_\alpha^2\alpha^2$, where $\alpha$ takes values $x$, $y$, and $z$. We introduce the following creation and annihilation operators:

$$a_\alpha^\dagger \equiv \frac{1}{\sqrt{2}}\left(\frac{\alpha}{d_\alpha} - d_\alpha\frac{\partial}{\partial\alpha}\right),$$

$$a_\alpha \equiv \frac{1}{\sqrt{2}}\left(\frac{\alpha}{d_\alpha} + d_\alpha\frac{\partial}{\partial\alpha}\right), \tag{A2}$$

where $d_\alpha\equiv\sqrt{\hbar/m\omega_\alpha}$. The introduced operators satisfy the bosonic commutation relation

$$[a_\alpha, a_{\alpha'}^\dagger] = \delta_{\alpha,\alpha'}, \quad [a_\alpha, a_\alpha] = [a_\alpha^\dagger, a_{\alpha'}^\dagger] = 0. \tag{A3}$$

Using this notation, the single-particle Hamiltonian can be written in the form

$$H_0(\boldsymbol{r}) = \sum_\alpha \hbar\omega_\alpha\left(a_\alpha^\dagger a_\alpha + \frac{1}{2}\right). \tag{A4}$$

We denote the order parameter for an arbitrary spin-$F$ BEC with the $(2F+1)$-dimensional vector,

$$\boldsymbol{\Psi}(\boldsymbol{r}) = (\Psi_F(\boldsymbol{r}), \Psi_{F-1}(\boldsymbol{r}), \ldots, \Psi_{-F}(\boldsymbol{r}))^T. \tag{A5}$$

The GP equation can be written in a general form,

$$[H_0(\boldsymbol{r})\underline{\tau}_0 + \underline{\Sigma}(\boldsymbol{r})]\boldsymbol{\Psi}(\boldsymbol{r}) + \underline{\tilde{\Delta}}(\boldsymbol{r})\boldsymbol{\Psi}^*(\boldsymbol{r}) = \mu\boldsymbol{\Psi}(\boldsymbol{r}). \tag{A6}$$

Here the $(2F+1)$-dimensional square matrices $\underline{\Sigma}(\boldsymbol{r})$ and $\underline{\tilde{\Delta}}(\boldsymbol{r})$ are local self-energies. A $(2F+1)$-dimensional unit matrix $\underline{\tau}_0\equiv\mathrm{diag}(1,\ldots,1)$ is also introduced. From Eq. (A6) we obtain a set of two equations,

$$[\hat{H}_0(\boldsymbol{r}) - \hbar\omega_\alpha\hat{\tau}_0]\begin{bmatrix} a_\alpha^\dagger\boldsymbol{\Psi}(\boldsymbol{r}) \\ a_\alpha\boldsymbol{\Psi}^*(\boldsymbol{r}) \end{bmatrix} = \begin{bmatrix} -\{a_\alpha^\dagger\underline{\Sigma}(\boldsymbol{r})\}\boldsymbol{\Psi}(\boldsymbol{r}) \\ \{a_\alpha\underline{\Sigma}^*(\boldsymbol{r})\}\boldsymbol{\Psi}^*(\boldsymbol{r}) \end{bmatrix} + \begin{bmatrix} -a_\alpha^\dagger\{\underline{\tilde{\Delta}}(\boldsymbol{r})\}\boldsymbol{\Psi}^*(\boldsymbol{r}) \\ a_\alpha\{\underline{\tilde{\Delta}}^*(\boldsymbol{r})\boldsymbol{\Psi}(\boldsymbol{r})\} \end{bmatrix}. \tag{A7}$$

Here we introduce $\hat{\tau}_0\equiv\mathrm{diag}(\underline{\tau}_0,\underline{\tau}_0)$ and a $[2\times(2F+1)]$-dimensional square matrix $\hat{H}_0$,

$$\hat{H}_0(\boldsymbol{r}) \equiv \mathrm{diag}[\{H_0(\boldsymbol{r})-\mu\}\underline{\tau}_0 + \underline{\Sigma}(\boldsymbol{r}) - \{H_0(\boldsymbol{r})-\mu\}\underline{\tau}_0 - \underline{\Sigma}^*(\boldsymbol{r})]. \tag{A8}$$

From Eq. (A5) one can derive the general form of the BdG equation,

$$\hat{H}_0\begin{bmatrix}\boldsymbol{u}_\nu(\boldsymbol{r})\\ \boldsymbol{v}_\nu(\boldsymbol{r})\end{bmatrix} + \begin{bmatrix}\underline{\Delta}(\boldsymbol{r})\boldsymbol{v}_\nu(\boldsymbol{r})\\ -\underline{\Delta}^*(\boldsymbol{r})\boldsymbol{u}_\nu(\boldsymbol{r})\end{bmatrix} = E_\nu\begin{bmatrix}\boldsymbol{u}_\nu(\boldsymbol{r})\\ \boldsymbol{v}_\nu(\boldsymbol{r})\end{bmatrix}. \tag{A9}$$

At zero temperature, $\underline{\Delta}(\boldsymbol{r})$ is equal to $\underline{\tilde{\Delta}}(\boldsymbol{r})$ in the GP equation. Let us take an ansatz

$$\begin{bmatrix}\boldsymbol{u}_{\nu=\alpha}(\boldsymbol{r})\\ \boldsymbol{v}_{\nu=\alpha}(\boldsymbol{r})\end{bmatrix} = \begin{bmatrix}a_\alpha^\dagger\boldsymbol{\Psi}(\boldsymbol{r})\\ a_\alpha\boldsymbol{\Psi}^*(\boldsymbol{r})\end{bmatrix}, \tag{A10}$$

and write the BdG equation using Eq. (A7) in the form

$$(E_\alpha - \hbar\omega_\alpha)\begin{bmatrix} a_\alpha^\dagger \boldsymbol{\Psi}(\boldsymbol{r}) \\ a_\alpha \boldsymbol{\Psi}^*(\boldsymbol{r}) \end{bmatrix} = \begin{bmatrix} -\{a_\alpha^\dagger \underline{\Sigma}(\boldsymbol{r})\}\boldsymbol{\Psi}(\boldsymbol{r}) - a_\alpha^\dagger\{\underline{\Delta}(\boldsymbol{r})\boldsymbol{\Psi}^*(\boldsymbol{r})\} + \underline{\Delta}(\boldsymbol{r})a_\alpha \boldsymbol{\Psi}^*(\boldsymbol{r}) \\ \{a_\alpha \underline{\Sigma}^*(\boldsymbol{r})\}\boldsymbol{\Psi}^*(\boldsymbol{r}) + a_\alpha\{\underline{\Delta}^*(\boldsymbol{r})\boldsymbol{\Psi}(\boldsymbol{r})\} - \underline{\Delta}^*(\boldsymbol{r})a_\alpha^\dagger \boldsymbol{\Psi}(\boldsymbol{r}) \end{bmatrix}. \tag{A11}$$

All results above are for a general BEC with hyperfine spin $F$. Below, we restrict the discussion to the $F=1$ case since the self-energy for this case is known. Here, the order parameter takes the form $\boldsymbol{\Psi}(\boldsymbol{r})=(\Psi_1(\boldsymbol{r}),\Psi_0(\boldsymbol{r}),\Psi_{-1}(\boldsymbol{r}))^T$. Using the notation [64]

$$\underline{A}^\nu \equiv \begin{cases} \underline{\tau}_0 & \text{for } \nu=0, \\ \underline{F}^\nu & \text{for } \nu=1,2,3, \end{cases} \tag{A12}$$

$$g_\nu \equiv \begin{cases} g_n' & \text{for } \nu=0, \\ g_s' & \text{for } \nu=1,2,3, \end{cases} \tag{A13}$$

the self-energies are written as

$$\underline{\Sigma}(\boldsymbol{r}) = g_\nu[\boldsymbol{\Psi}^\dagger(\boldsymbol{r})\underline{A}^\nu\boldsymbol{\Psi}(\boldsymbol{r})\underline{A}^\nu + \underline{A}^\nu\boldsymbol{\Psi}(\boldsymbol{r})\boldsymbol{\Psi}^\dagger(\boldsymbol{r})\underline{A}^\nu], \tag{A14}$$

$$\underline{\Delta}(\boldsymbol{r}) = -g_\nu \underline{A}^\nu\boldsymbol{\Psi}(\boldsymbol{r})[\boldsymbol{\Psi}^\dagger(\boldsymbol{r})\underline{A}^\nu]^*, \tag{A15}$$

where summation over repeated superscripts is implied. We substitute these self-energies in the BdG equation (A11), and using the condition $[\boldsymbol{\Psi}^\dagger\underline{A}^\nu\boldsymbol{\Psi}]^*=\boldsymbol{\Psi}^\dagger\underline{A}^\nu\boldsymbol{\Psi}$ we finally observe that

$$(E_\alpha - \hbar\omega_\alpha)\begin{bmatrix} a_\alpha^\dagger \boldsymbol{\Psi}(\boldsymbol{r}) \\ a_\alpha \boldsymbol{\Psi}^*(\boldsymbol{r}) \end{bmatrix} = \begin{bmatrix} \boldsymbol{\eta}(\boldsymbol{r}) \\ -\boldsymbol{\eta}^*(\boldsymbol{r}) \end{bmatrix}, \tag{A16}$$

where we have defined

$$\boldsymbol{\eta}(\boldsymbol{r}) \equiv -\{a_\alpha^\dagger \underline{\Sigma}(\boldsymbol{r})\}\boldsymbol{\Psi}(\boldsymbol{r}) - a_\alpha^\dagger\{\underline{\Delta}(\boldsymbol{r})\boldsymbol{\Psi}^*(\boldsymbol{r})\} + \underline{\Delta}(\boldsymbol{r})a_\alpha\boldsymbol{\Psi}^*(\boldsymbol{r}).$$

Assuming that $E_\alpha$ is real, Eq. (A16) yields

$$(E_\alpha - \hbar\omega_\alpha)(a_\alpha^\dagger + a_\alpha)\boldsymbol{\Psi}(\boldsymbol{r}) = \mathbf{0}. \tag{A17}$$

Since $(a_\alpha^\dagger + a_\alpha)\boldsymbol{\Psi}(\boldsymbol{r}) \neq 0$, we conclude that there always exists a mode with energy $E_\alpha=\hbar\omega_\alpha$. Therefore the Kohn mode exists irrespective of the atom-atom interactions. The eigenvector and eigenenergy are given by $E_\alpha=\hbar\omega_\alpha$ and $(\boldsymbol{u}_\nu,\boldsymbol{v}_\nu)^T = (a_\alpha^\dagger\boldsymbol{\Psi}(\boldsymbol{r}), a_\alpha\boldsymbol{\Psi}^*(\boldsymbol{r}))^T$, respectively. In our numerical calculations, we typically find the dipole mode with a relative error of less than $1.5\times10^{-5}$.


[1] M. H. Anderson, J. R. Ensher, M. R. Mathews, C. E. Wieman, and E. A. Cornell, Science **269**, 198 (1995).
[2] C. C. Bradley, C. A. Sackett, J. J. Tollett, and R. G. Hulet, Phys. Rev. Lett. **75**, 1687 (1995).
[3] K. B. Davis, M.-O. Mewes, M. R. Andrews, N. J. van Druten, D. S. Durfee, D. M. Kurn, and W. Ketterle, Phys. Rev. Lett. **75**, 3969 (1995).
[4] C. J. Pethick and H. Smith, *Bose-Einstein Condensation in Dilute Gases* (Cambridge University Press, Cambridge, England, 2002).
[5] *Bose-Einstein Condensation in Atomic Gases*, edited by M. Inguscio, S. Stringari, and C. E. Wieman (IOS Press, Amsterdam, 1999).
[6] *Coherent Atomic Matter Waves*, edited by R. Kaiser, C. Westbrook, and F. David, Proceedings of the Les Houches Summer School of Theoretical Physics, LXXII (Springer-Verlag, Berlin, 2001).
[7] I. Bloch, J. Dalibard, and W. Zwerger, Rev. Mod. Phys. **80**, 885 (2008).
[8] T. Ohmi and K. Machida, J. Phys. Soc. Jpn. **67**, 1822 (1998).
[9] T.-L. Ho, Phys. Rev. Lett. **81**, 742 (1998).
[10] J. Stenger, S. Inouye, D. M. Stamper-Kurn, H.-J. Miesner, A. P. Chikkatur, and W. Ketterle, Nature (London) **396**, 345 (1998).
[11] A. Görlitz, T. L. Gustavson, A. E. Leanhardt, R. Löw, A. P. Chikkatur, S. Gupta, S. Inouye, D. E. Pritchard, and W. Ketterle, Phys. Rev. Lett. **90**, 090401 (2003).
[12] M. Barrett, J. Sauer, and M. S. Chapman, Phys. Rev. Lett. **87**, 010404 (2001).
[13] H. Schmaljohann, M. Erhard, J. Kronjäger, M. Kottke, S. van Staa, L. Cacciapuoti, J. J. Arlt, K. Bongs, and K. Sengstock, Phys. Rev. Lett. **92**, 040402 (2004).
[14] M.-S. Chang, C. D. Hamley, M. D. Barrett, J. A. Sauer, K. M. Fortier, W. Zhang, L. You, and M. S. Chapman, Phys. Rev. Lett. **92**, 140403 (2004).
[15] T. Kuwamoto, K. Araki, T. Eno, and T. Hirano, Phys. Rev. A **69**, 063604 (2004).
[16] A. E. Leanhardt, Y. Shin, D. Kielpinski, D. E. Pritchard, and W. Ketterle, Phys. Rev. Lett. **90**, 140403 (2003).
[17] K. C. Wright, L. S. Leslie, and N. P. Bigelow, Phys. Rev. A **77**, 041601(R) (2008).
[18] S.-K. Yip, Phys. Rev. Lett. **83**, 4677 (1999).
[19] T. Isoshima, K. Machida, and T. Ohmi, J. Phys. Soc. Jpn. **70**, 1604 (2001).
[20] T. Isoshima, M. Nakahara, T. Ohmi, and K. Machida, Phys. Rev. A **61**, 063610 (2000).
[21] M. Nakahara, T. Isoshima, K. Machida, S. Ogawa, and T. Ohmi, Physica B **284-288**, 17 (2000).
[22] T. Isoshima and K. Machida, Phys. Rev. A **66**, 023602 (2002).
[23] U. Leonhardt and G. E. Volovik, Pis'ma Zh. Eksp. Teor. Fiz. **72**, 66 (2000) [JETP Lett. **72**, 46 (2000)].
[24] H. T. C Stoof, e-print arXiv:cond-mat/0002375.
[25] K.-P. Marzlin, W. Zhang, and B. C. Sanders, Phys. Rev. A **62**, 013602 (2000).
[26] T. Mizushima, K. Machida, and T. Kita, Phys. Rev. Lett. **89**, 030401 (2002).
[27] T. Mizushima, K. Machida, and T. Kita, Phys. Rev. A **66**, 053610 (2002).
[28] T. Mizushima, N. Kobayashi, and K. Machida, Phys. Rev. A **70**, 043613 (2004).
[29] J.-P. Martikainen, A. Collin, and K.-A. Suominen, Phys. Rev. A **66**, 053604 (2002).

[30] V. Pietilä, M. Möttönen, and S. M. M. Virtanen, Phys. Rev. A **76**, 023610 (2007).
[31] N. D. Mermin and T.-L. Ho, Phys. Rev. Lett. **36**, 594 (1976).
[32] P. W. Anderson and G. Toulouse, Phys. Rev. Lett. **38**, 508 (1977).
[33] P. J. Hakonen, O. T. Ikkala, S. T. Islander, O. V. Lounasmaa, and G. E. Volovik, J. Low Temp. Phys. **53**, 425 (1983).
[34] R. Blaauwgeers, V. B. Eltsov, M. Krusius, J. J. Ruohio, R. Schanen, and G. E. Volovik, Nature (London) **404**, 471 (2000).
[35] F. Zhou, Phys. Rev. Lett. **87**, 080401 (2001).
[36] N. P. Robins, W. Zhang, E. A. Ostrovskaya, and Y. S. Kivshar, Phys. Rev. A **64**, 021601(R) (2001).
[37] See also, K. Kasamatsu, M. Tsubota, and M. Ueda, Int. J. Mod. Phys. B **19**, 1835 (2005).
[38] C. V. Ciobanu, S.-K. Yip, and T.-L. Ho, Phys. Rev. A **61**, 033607 (2000).
[39] M. Koashi and M. Ueda, Phys. Rev. Lett. **84**, 1066 (2000).
[40] J.-P. Martikainen and K.-A. Suominen, J. Phys. B **34**, 4091 (2001).
[41] W. V. Pogosov, R. Kawate, T. Mizushima, and K. Machida, Phys. Rev. A **72**, 063605 (2005).
[42] M. Ueda and M. Koashi, Phys. Rev. A **65**, 063602 (2002).
[43] M. Möttönen, N. Matsumoto, M. Nakahara, and T. Ohmi, J. Phys.: Condens. Matter **14**, 13481 (2002).
[44] H. Mäkelä, Y. Zhang, and K.-A. Suominen, J. Phys. A **36**, 8555 (2003).
[45] G. W. Semenoff and F. Zhou, Phys. Rev. Lett. **98**, 100401 (2007).
[46] H. Pu, C. K. Law, J. H. Eberly, and N. P. Bigelow, Phys. Rev. A **59**, 1533 (1999).
[47] M. Möttönen, T. Mizushima, T. Isoshima, M. M. Salomaa, and K. Machida, Phys. Rev. A **68**, 023611 (2003).
[48] J. A. M. Huhtamäki, M. Möttönen, and S. M. M. Virtanen, Phys. Rev. A **74**, 063619 (2006).
[49] E. Lundh and H. M. Nilsen, Phys. Rev. A **74**, 063620 (2006).
[50] Y. Kawaguchi and T. Ohmi, Phys. Rev. A **70**, 043610 (2004).
[51] S. Stringari, Phys. Rev. Lett. **77**, 2360 (1996).
[52] F. Zambelli and S. Stringari, Phys. Rev. Lett. **81**, 1754 (1998).
[53] Y. Shin, M. Saba, M. Vengalattore, T. A. Pasquini, C. Sanner, A. E. Leanhardt, M. Prentiss, D. E. Pritchard, and W. Ketterle, Phys. Rev. Lett. **93**, 160406 (2004).
[54] J. A. M. Huhtamäki, M. Möttönen, T. Isoshima, V. Pietilä, and S. M. M. Virtanen, Phys. Rev. Lett. **97**, 110406 (2006).
[55] T. Isoshima, M. Okano, H. Yasuda, K. Kasa, J. A. M. Huhtamäki, M. Kumakura, and Y. Takahashi, Phys. Rev. Lett. **99**, 200403 (2007).
[56] M. Mine, M. Okumura, T. Sunaga, and Y. Yamanaka, Ann. Phys. (N.Y.) **322**, 2327 (2007).
[57] T. Sunaga, K. Misawa, M. Mine, and Y. Yamanaka (private communication).
[58] N. N. Klausen, J. L. Bohn, and C. H. Greene, Phys. Rev. A **64**, 053602 (2001).
[59] A. Crubellier, O. Dulieu, F. Masnou-Seeuws, M. Elbs, H. Knockel, and E. Tiemann, Eur. Phys. J. D **6**, 211 (1999).
[60] J. F. Dobson, Phys. Rev. Lett. **73**, 2244 (1994).
[61] A. L. Fetter and D. Rokhsar, Phys. Rev. A **57**, 1191 (1998).
[62] W. Kohn, Phys. Rev. **123**, 1242 (1961).
[63] M. Möttönen, S. M. M. Virtanen, and M. M. Salomaa, Phys. Rev. A **71**, 023604 (2005).
[64] Y. Kondo and T. Kita, J. Phys. Soc. Jpn. **76**, 024008 (2007).